Title

The influence of processing methods on creep of wrought and additively manufactured CrCoNi multi-principal element alloys

Authors

Sahragard-Monfared, Gianmarco

Zhang, Mingwei

Smith, Timothy M

et al.

Publication Date

2023-12-01

DOI

10.1016/j.actamat.2023.119403

Acta Materialia 261 (2023) 119403

Contents lists available at ScienceDirect

Acta Materialia

journal homepage: www.elsevier.com/locate/actamat

The influence of processing methods on creep of wrought and additively manufactured CrCoNi multi-principal element alloys

Gianmarco Sahragard-Monfared [a], Mingwei Zhang [b,c], Timothy M. Smith [d], Andrew M. Minor [b,c], Easo P. George [e,f], Jeffery C. Gibeling [a,*]

[a] Department of Materials Science and Engineering, University of California, One Shields Avenue, Davis, CA 95616, USA
[b] National Center for Electron Microscopy, Molecular Foundry, Lawrence Berkeley National Laboratory, 1 Cyclotron Road, Berkeley, California 94720, USA
[c] Department of Materials Science and Engineering, University of California, 2607 Hearst Avenue, Berkeley, California 94720, USA
[d] High Temperature and Smart Alloys Branch, NASA Glenn Research Center, 21000 Brookpark Rd., Cleveland, Ohio 44135, USA
[e] Materials Science and Technology Division, Oak Ridge National Laboratory, 1 Bethel Valley Road, Oak Ridge, Tennessee 37831, USA
[f] Materials Science and Engineering Department, University of Tennessee, 1508 Middle Drive, Knoxville, TN 37996, USA

ARTICLE INFO

Keywords:
CrCoNi
Creep
Multi-principal element alloys
Oxides
Grain boundaries

ABSTRACT

The influence of vacuum arc melting and mechanical processing (wrought) versus additive manufacturing (AM) on the creep behavior of multi-principal element alloys (MPEA) is investigated in this study. Annealed wrought and hot isostatically pressed (HIP) AM CrCoNi were creep tested under constant tensile stress of 40 to 200 MPa at temperatures of 1023 to 1173 K. Stress exponents of 4.5 ± 0.2 and 5.9 ± 0.1 and activation energies ranging from 240 to 259 and 320 to 331 kJ/mol were found for wrought and AM CrCoNi, respectively. The results indicate that the AM material exhibits superior creep resistance and inferior creep ductility compared to the wrought alloy. This difference is attributed to the AM material having a higher percentage of Cr-rich oxides, a smaller total low angle grain boundary (LAGB) length on a percentage basis, and a greater total twin boundary (TB) length on a percentage basis. The AM and wrought materials have similar grain sizes; however, the smaller LAGB length and greater TB length in the AM material reduce slip transmission on the other side of the boundaries and contribute to strength. The dislocation structures of the AM and wrought materials consist of individual curved dislocations with dislocation multijunctions and jogs, which is similar to the arrangements previously observed in CrMnFeCoNi.

1. Introduction

Multi-principal element alloys (MPEA) are materials in which three to five elements are present at high concentrations and often in roughly equal proportions. The most extensively studied FCC MPEAs are equiatomic CrMnFeCoNi (Cantor alloy) and a derivative, CrCoNi, which have been proven to exhibit excellent room temperature and cryogenic strength and ductility [1–4]. Studies have shown that CrMnCoNi has the highest yield strength, and the Cantor alloy achieves the highest ductility, whereas CrCoNi displays the best combination of strength, ductility, and damage tolerance [5,6]. This favorable combination of properties has been attributed to the formation of nanotwin-HCP lamellae that partition grains into much smaller structural units that can sustain large lattice rotations and contribute to extensive strain hardening [4]. However, limited resistance to deformation at high temperatures has constrained the range of applications of MPEAs to date [7–10].

In order to enhance high temperature and other material properties, several investigators have added Ti, Al, and other elements to essentially create high entropy superalloys similar to conventional Ni-based superalloys [11–15]. However, this method does not take full advantage of the unique aspects of MPEA compositions. As an alternative, a recent study by Hadraba, et al. of oxide dispersion strengthened (ODS) Cantor alloy has shown that it is possible to retain the MPEA matrix with the addition of dispersoids to provide good high temperature strength. Hadraba, et al. fabricated the ODS alloy by adding O_2 gas, Y, and Ti to the blend of Cantor alloy powders during mechanical alloying and subsequently spark plasma sintered the alloyed powders [16]. Recently, Smith, et al. have successfully used laser powder bed fusion (L-PBF) of acoustically mixed yttria coated CrCoNi particles to create additively

* Corresponding author.
E-mail address: jcgibeling@ucdavis.edu (J.C. Gibeling).

https://doi.org/10.1016/j.actamat.2023.119403
Received 6 July 2023; Received in revised form 30 September 2023; Accepted 1 October 2023
Available online 5 October 2023

manufactured (AM) ODS CrCoNi [17]. With the advancement of AM as a novel economically viable method for combining the dispersoids and metal matrix, the new feasibility of dispersion strengthening makes it an excellent solution for overcoming the high temperature limitations of FCC MPEAs.

It is well known that processing methods such as vacuum arc melting (VAM), spark plasma sintering (SPS), and AM produce alloys with varying mechanical properties. Yang, et al. investigated processing effects of VAM, SPS, and hot-press sintering on an FeCrNiAl medium entropy alloy and found significant differences in microstructure, mechanical properties, and strengthening mechanisms among the methods [18]. However, the effect of processing methods on tensile creep properties has not been investigated thus far. To address this shortcoming and as a first step toward understanding the matrix properties of potential ODS MPEAs, this study focuses on a comparison of the initial and deformed microstructures, creep properties, and failure mechanisms of wrought and AM CrCoNi.

2. Experimental methods

Wrought CrCoNi was fabricated by arc-melting and drop casting under pure Ar atmosphere. The arc-melted buttons were flipped, remelted five times to promote homogeneity, and drop cast into a copper mold, similar to the process described for the Cantor alloy by Otto, et al. [19]. After casting, the material was homogenized under vacuum at 1473 K for 24 h. It then underwent a ~95 % thickness reduction via cold rolling to a final thickness of 1 mm. The AM CrCoNi was fabricated by L-PBF of pre-alloyed equiatomic CrCoNi powder with a diameter range between 10 - 45 μm, as described by Smith, et al. [17]. Two 99.9 % dense blanks of AM CrCoNi with a geometry of 88.9 (L) x 15.88 (W) x 15.88 (T) mm were fabricated in a single build and then HIPed at 1458 K to relieve residual stress, remove any defects caused from the AM process, and form a more equiaxed grain structure.

The compositions of the two materials were measured by solid state infrared absorption using a LECO CS-444-LS carbon/sulfur determinator and by inert gas fusion in a LECO TC-436 nitrogen/oxygen determinator, both with resolutions of less than 1 ppm per element. A Varian Vista Pro-Inductively Coupled Plasma Emission Spectrometer was used to measure the metallic elements. The compositions of both materials are listed in Table 1. The data include common elements that are known to affect ductility of nickel-based superalloys. As shown in the table, the levels of sulfur, carbon, nitrogen, and magnesium are low and essentially the same in the two alloys. However, the AM material contains a greater concentration of oxygen, which was most likely present on the surfaces of the starting powders or introduced in the build chamber.

Tensile creep specimens (Fig. 1), with 35.56 (L) x 2.54(W) x 1.00(T) mm gage dimensions were electrical discharge machined from the wrought sheet and AM builds. The wrought and AM CrCoNi specimens were cut such that the tensile axis (Z-direction) is parallel to the rolling and build directions, respectively. The wrought specimens were annealed in vacuum at 1173 K for 6 h to achieve an average grain size similar to that of the HIPed AM CrCoNi in order to limit the influence of grain size in this study. Most of the AM specimens were tested in the HIPed condition, but four additional AM specimens were annealed in vacuum at 1173 K for 6 h to minimize initial dislocation density. All specimens were polished using SiC papers to 600 grit on the surfaces and edges of the gage sections to minimize the risk of surface defects influencing the creep data.

Scanning electron microscopy (SEM) was performed on a Thermo Fisher Quattro S SEM and an FEI Scios Dual Beam FIB/SEM equipped with EDS and EBSD detectors. All microscopy samples were prepared by grinding and polishing to 0.3 μm with an alumina suspension and then vibropolishing with 0.05 μm colloidal silica for 4 h. The Quattro SEM was used in backscatter electron (BSE) mode to characterize the fractured specimens and grain morphologies. The Scios FIB/SEM was used to characterize the atomic compositions of each material via energy dispersive x-ray spectroscopy (EDS) and the grain orientations and boundary misorientations via electron backscatter diffraction (EBSD). EDS was performed at an operating voltage of 30 kV and EBSD was performed at an operating voltage of 15 kV and step size of 0.8 μm. The EBSD data were post-processed with MTEX (version 5.7.0) in MATLAB following a procedure similar to that used by Broyles, et al. [20] such that unreasonably small grains are removed and unindexed data points are filled based on the orientations of their neighbors. Average grain size was determined from the boundary misorientation maps using the line intercept method and excluding twin boundaries (TB). Crystallite size, as adopted from Schneider, et al., considers both annealing TBs and grain boundaries [21], and was also determined using the line intercept method on the boundary misorientation maps.

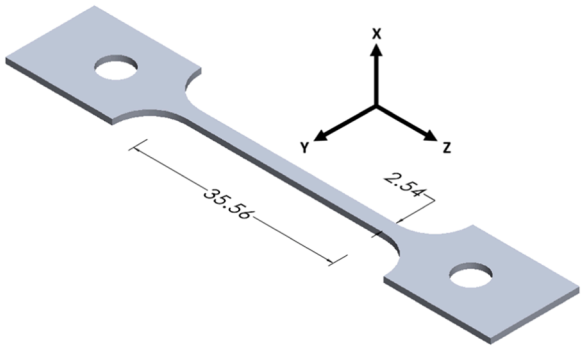

Fig. 1. Isometric view of a creep specimen. All dimensions are in mm.

Transmission electron microscopy (TEM) samples in the YZ plane were prepared by grinding and polishing the specimen gage surface to 1200 grit and less than 100 μm thickness. The TEM samples were then twin jet polished using a Fischione Model 110 Automatic Twin-Jet Electropolisher with a 70 % methanol, 20 % glycerol, and 10 % perchloric acid solution. The dislocation structures of the crept specimens were studied by TEM performed on a JEOL 3010 TEM at an accelerating voltage of 300 kV and diffraction contrast imaging scanning TEM (DCI-STEM) conducted on an FEI Tecnai S/TEM at an accelerating voltage of 200 kV. Scanning TEM EDS (STEM-EDS) was performed on an FEI TitanX to identify the composition of particles in the AM CrCoNi.

Constant stress tensile creep tests were performed under vacuum ($\leq 3 \times 10^{-5}$ torr) to avoid oxidation, following the procedures described by Decker, et al. [21]. Tests were performed in the ranges of 1023–1173 K and 40–200 MPa and were conducted until fracture to ensure each specimen reached steady state creep. Two sets of interrupted tests were also performed for each material. One set was terminated once steady state had been achieved, and specimens were furnace cooled under load to preserve the dislocation structure for TEM. The other set was terminated at 4 % strain to compare the extent of cracking in the two materials at a common strain prior to fracture.

Table 1
Alloy Compositions of Key Elements in wt %.

MATERIAL	Cr	Co	Ni	C	O	N	S	Mg
Wrought CrCoNi	30.4	34.7	34.8	0.00125	0.0138	0.0005	0.00065	0.0020
AM CrCoNi	30.2	34.7	34.9	0.00125	0.0563	0.0038	0.00085	0.0030

3. Results and discussion

3.1. Characterization of initial microstructure

Wrought and AM MPEAs have been observed to have a uniform distribution of elements, however, verification of an evenly distributed matrix of elements in both materials is critical to this comparative study [22,23]. Hence, the initial chemical composition of both materials was determined by SEM-EDS as shown in Fig. S1, where both were observed to be equiatomic with a uniform distribution of the three principal elements. The EBSD images and inverse pole figure (IPF) contour plots displayed in Fig. 2 illustrate that there is minimal texture in both materials. The IPF contour plot shown for the AM material was generated from the EBSD map of the YZ plane and is also representative of the IPF contour plot of the EBSD map of the XY plane. Both materials have a significant number of annealing twins, which is typical for this alloy [24,25].

Fig. 3 shows the boundary misorientation plots of wrought CrCoNi, XY AM CrCoNi, and YZ AM CrCoNi from which grain sizes and crystallite sizes were determined. The grains in the wrought CrCoNi are equiaxed with a grain size of 31.2 ± 1.9 μm and a crystallite size of 13.8 ± 2.1 μm. The AM CrCoNi grains are slightly elongated in the build direction with an irregular shape and aspect ratio of approximately 1.8:1 such that the grain size is 74.3 ± 2.6 μm in the Z-direction of the YZ plane and 41.4 ± 2.4 μm in the Y-direction of the YZ plane; the corresponding crystallite sizes are 22.0 ± 2.2 μm and 13.7 ± 2.1 μm. As noted by Smith, et al., the HIP cycle has allowed grains in the AM CrCoNi to partially recrystallize and become more equiaxed while retaining features typical of AM grain morphologies [17]. Fig. 3(c) illustrates the smaller percentage of low angle grain boundary (LAGB, colored blue) length in the YZ plane of the AM material compared to the wrought material. The length percentages of TB, high angle grain boundary (HAGB), and LAGB are quantified in Table 2 for both materials. These boundaries are defined with misorientation angles of 60 ± 3° (TBs), greater than 15° excluding TBs (HAGBs), and 1 – 15° (LAGBs). Histograms of misorientation angles for both materials are shown in Fig. S2. The HAGBs and LAGBs described here exist in the material prior to creep deformation. Subgrain boundaries that form during creep by clustering of dislocations also have small misorientation angles (typically 1° or less) but are distinct in origin and nature from the pre-existing low angle grain boundaries.

3.2. Creep results

Representative creep curves at various temperatures and applied stresses are presented in Fig. 4. Both materials display creep behavior typical of pure metals and alloys that behave like pure metals with distinct normal primary, secondary, and tertiary regions (although the latter is difficult to see at the chosen scale of the plot for the applied stress and temperature).

The power law equation (Eq. (1)) describes the relationship between steady state creep rate, $\dot{\varepsilon}_{SS}$, and applied stress, σ, where A is a material constant that includes dislocation structure, Q_C represents the creep

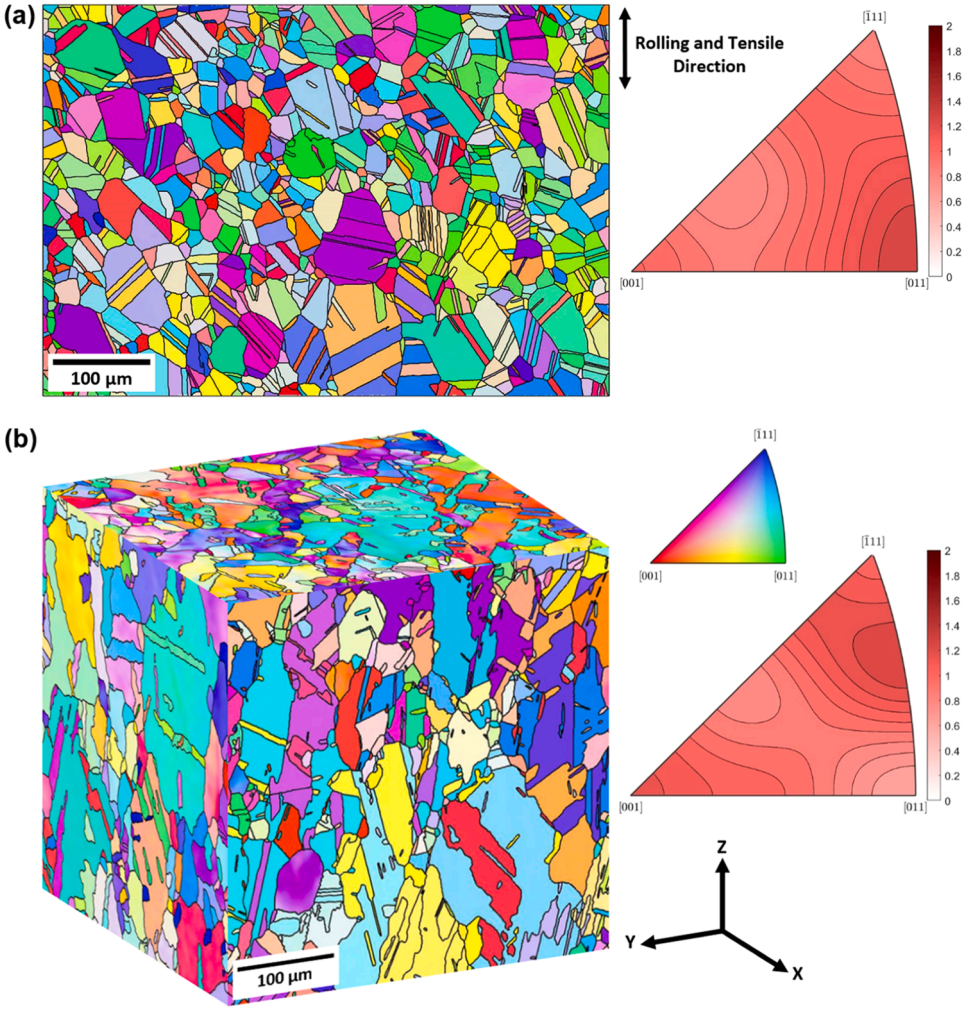

Fig. 2. EBSD-IPF color maps and IPF contour plots of (a) wrought CrCoNi (b) AM CrCoNi.

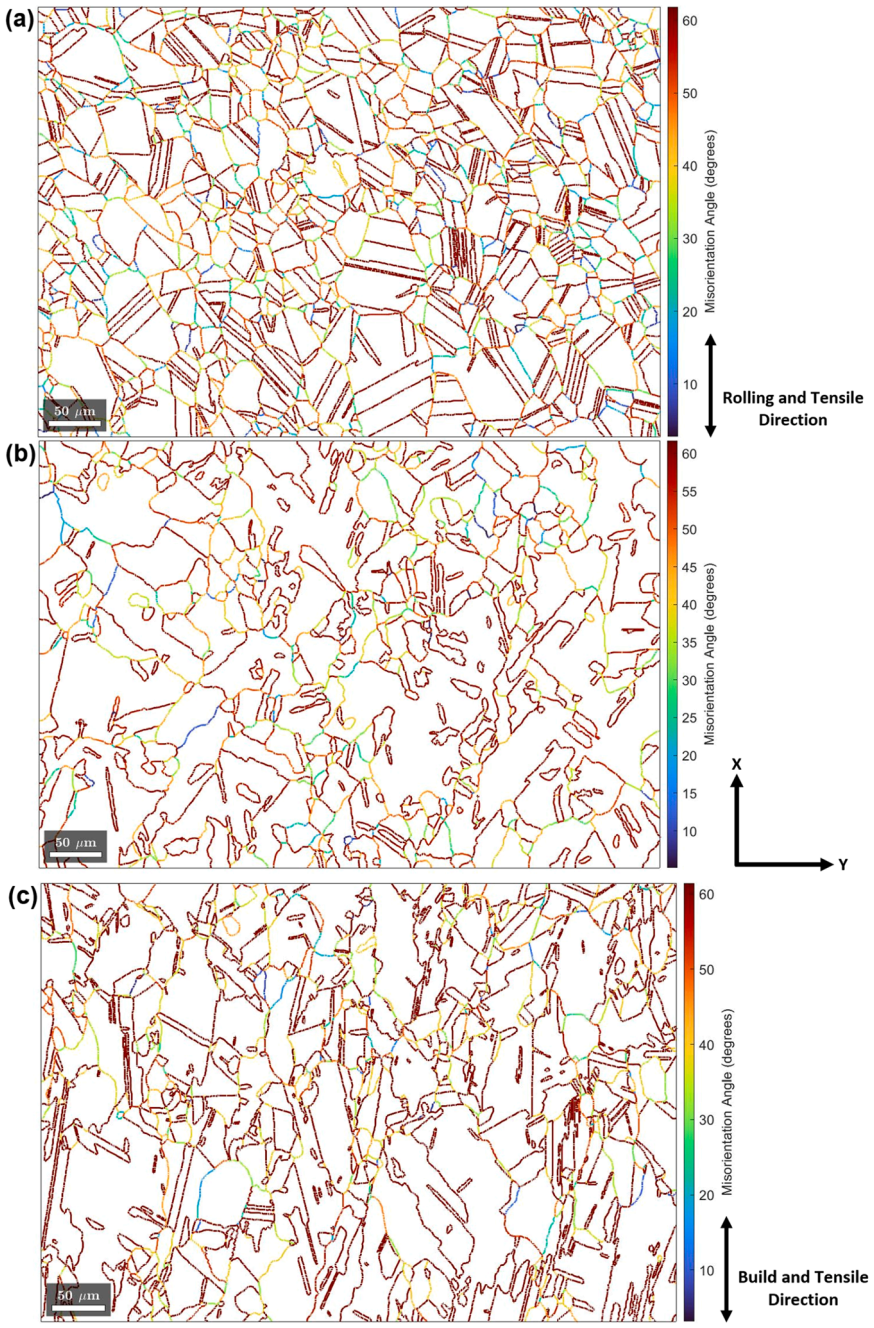

Fig. 3. Boundary misorientation plots of (a) wrought CrCoNi (b) XY plane of AM CrCoNi (c) YZ plane of AM CrCoNi.

Table 2
Percentages of Total Low Angle Grain Boundary, High Angle Grain Boundary, and Twin Boundary Length.

MATERIAL	LAGB	HAGB	TB
Wrought CrCoNi	3.2 %	41.9 %	54.9 %
AM CrCoNi (XY)	1.8 %	39.4 %	58.8 %
AM CrCoNi (YZ)	0.9 %	25.8 %	73.3 %

activation energy, R is the gas constant, and T is temperature [26].

$$\dot{\varepsilon}_{SS} = A\sigma^{n}\exp\left(-\frac{Q_C}{RT}\right) \quad (1)$$

Steady-state creep rates were obtained from the slopes of the secondary regions of the creep curves and plotted as a function of applied stress to determine the stress exponents for each material; this relationship is shown on double logarithmic plots in Fig. 5. Stress exponents of 4.5 ± 0.2 and 5.9 ± 0.1 were found for wrought and AM CrCoNi, respectively. These values are generally in the range commonly associated with the dislocation climb mechanism of creep deformation and the difference between them does not indicate a significant difference of mechanism. By comparing the two plots in Fig. 5, it is clear that AM CrCoNi exhibits a lower steady state creep rate than the wrought material for all but the two most extreme combinations of temperature and stress (200 MPa). To put these results in context, Fig. 6 provides a comparison of the steady-state creep rates and applied stresses (Fig. 6 (a)) and applied stresses normalized by the temperature dependent shear modulus (Fig. 6(b)) for wrought and AM CrCoNi along with data for the wrought high entropy Cantor alloy reported by Zhang, et al. at a single temperature of 1023 K [10]. These data illustrate that AM CrCoNi

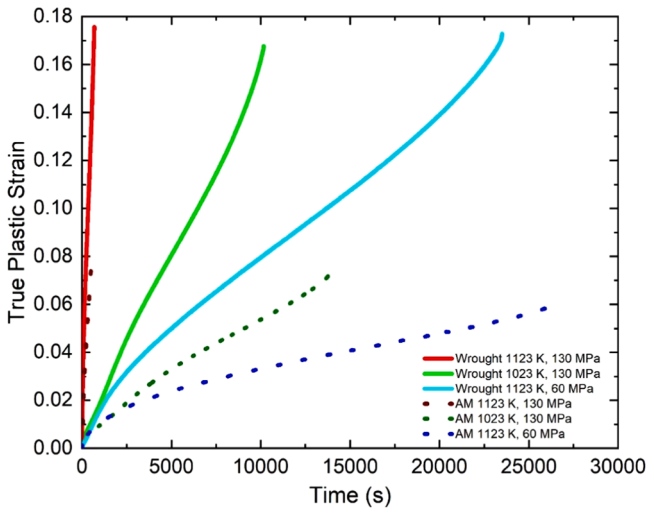

Fig. 4. Representative creep curves of wrought and AM CrCoNi.

has better creep resistance than wrought, and both have better creep resistance than the wrought Cantor alloy. The stress exponents of the CrCoNi are also higher than those found in the Cantor alloy when tested under similar conditions, implying that there may be different rate-controlling creep deformation mechanisms between CrCoNi and the Cantor alloy.

The activation energies of both materials were determined from a semi-log plot of steady state creep rate vs 1/T as shown in Fig. 7. The values range from 240 to 259 kJ/mol for wrought and 320–331 kJ/mol for AM CrCoNi reflecting the better creep resistance of the AM material. That is, at a given stress and temperature, the creep rate of the AM material is lower than that observed in the wrought material. While the activation energy for creep in the AM material agrees favorably with the reported self-diffusion activation energy of 330 kJ/mol, that is not the case for the wrought material which has a significantly lower creep activation energy [27]. The creep activation energies of both CrCoNi materials exceed that of the Cantor alloy, 219–236 kJ/mol [10].

Schneider, et al. reported that TBs contribute to boundary strengthening in low stacking fault energy alloys, such as CrCoNi, on the same scale as GBs [25]. Sun, et al. also found that TBs act as strong barriers to dislocation motion and hence play a key role in enhancing the creep resistance of CrCoNi [28]. In contrast, the orientation of grains on

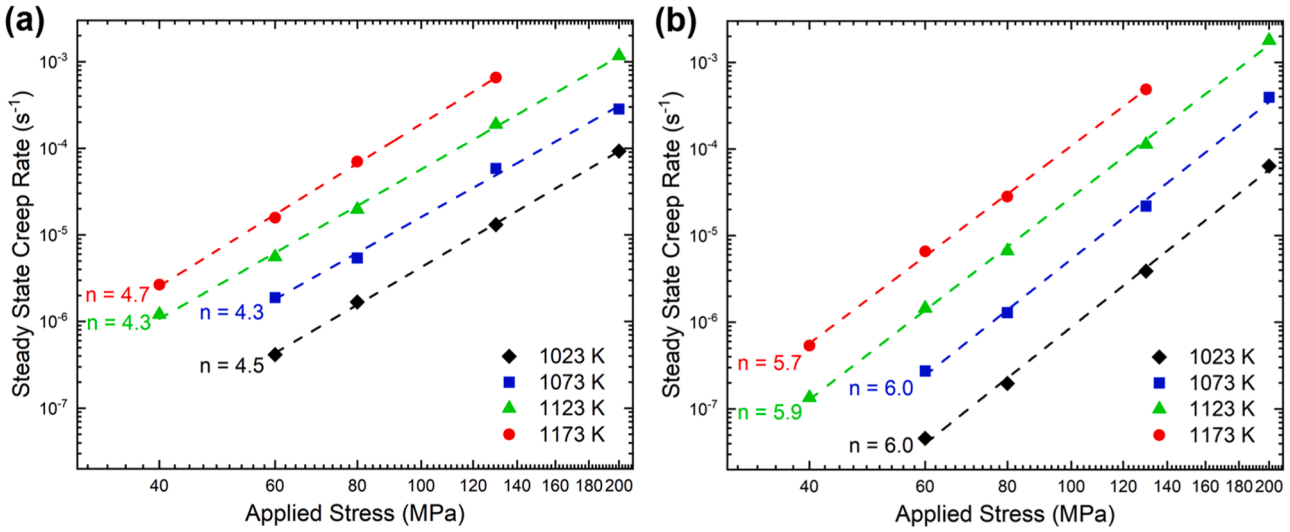

Fig. 5. Log-log plots of steady state creep rate vs applied stress for (a) wrought CrCoNi and (b) AM CrCoNi.

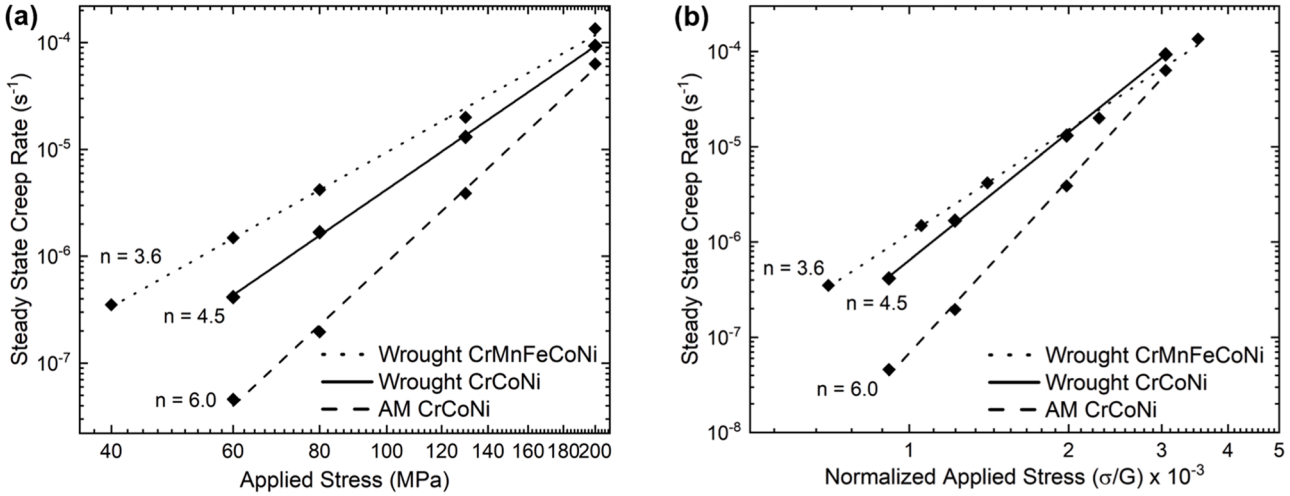

Fig. 6. Log-log plot of steady state creep rate as a function of (a) applied stress and (b) applied stress normalized by the temperature-dependent shear modulus for wrought Cantor alloy, wrought CrCoNi, and AM CrCoNi at 1023 K.

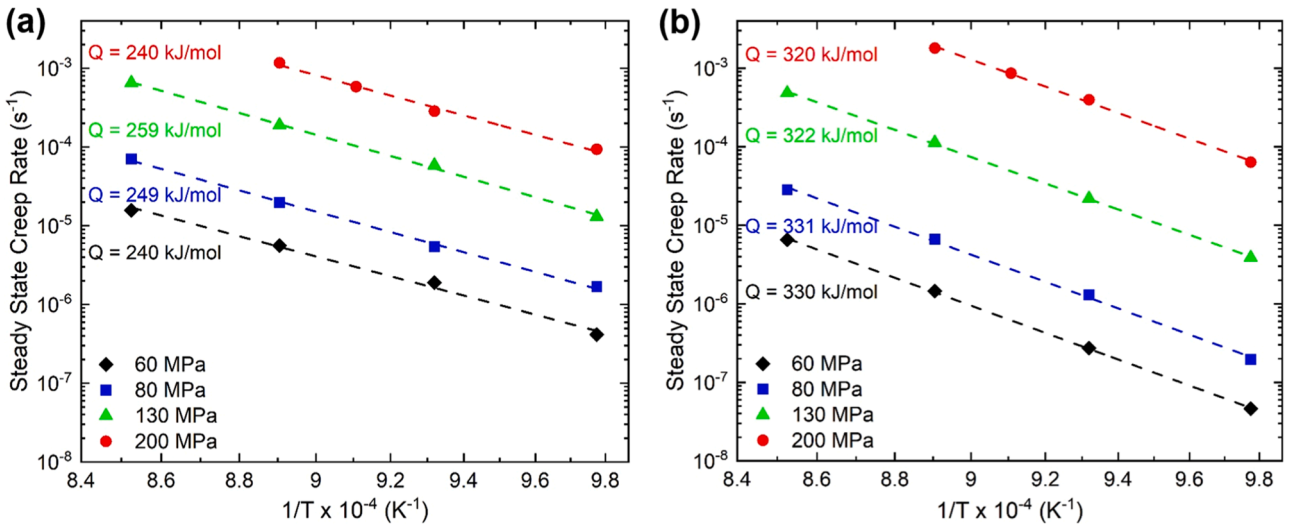

Fig. 7. Semi-log plot of steady state creep rate vs 1/T for (a) wrought CrCoNi and (b) AM CrCoNi.

each side of a LAGB is similar, allowing a smaller dislocation pile-up stress concentration in one grain to propagate deformation into the second grain [29,30]. Since the wrought material has more than twice as many LAGBs than the AM material, one reason for the difference in creep rates at a given stress and temperature is that lower stresses are required to propagate dislocation motion in the wrought material, contributing to its higher steady state creep rate than AM CrCoNi. Furthermore, as the stress increases, stronger barriers such as TBs are overcome, reducing the difference between AM and wrought, leading to a convergence of the data.

3.3. *Dislocation structures of wrought and AM CrCoNi*

In order to understand the origins of the difference in creep behaviors of wrought and AM CrCoNi, dislocation structures of the undeformed materials are presented in Figs. 8 and 9. The undeformed wrought material (Fig. 8(a)) exhibits a very low dislocation density as a result of the prior annealing (recrystallization) process. During the recovery stage of annealing, dislocation/dislocation annihilation and dislocation absorption at grain boundaries leads to a decreased dislocation density, which is further reduced during recrystallization. A twin boundary is also observed in Fig. 8(a). In contrast, one region of the dislocation structure in the undeformed AM material (Fig. 8(b)) reveals a high dislocation density as well as (111) slip traces and stacking faults. These dislocations are generated during the layer-by-layer build process of AM because of differential thermal expansion/contraction during heating and cooling of adjacent layers. Another region of the undeformed AM material (Fig. 9) shows a dislocation network, stacking fault tetrahedra (SFT), and extended nodes. SFT were first observed by Silcox and Hirsch in quenched gold and commonly originate from the collapse of vacancy clusters [31]. The SFT in the AM material likely formed due to the fast cooling rate of L-PBF which is similar to a quenching process. Particles are also observed in Figs. 8(b) and 9 and are discussed in the next section. Although both the wrought and AM materials were thermally processed at similar temperatures, the additional pressure of the HIPing process on the AM material does not allow for recovery of the dislocation structure.

It is well known that in pure polycrystalline FCC metals the transition from primary to secondary creep is caused by a decrease in mobile dislocation density typically associated with dislocations clustering into dense subgrain boundaries [32]. It is important to note that creep subgrain formation was not observed in either material, as is evident from

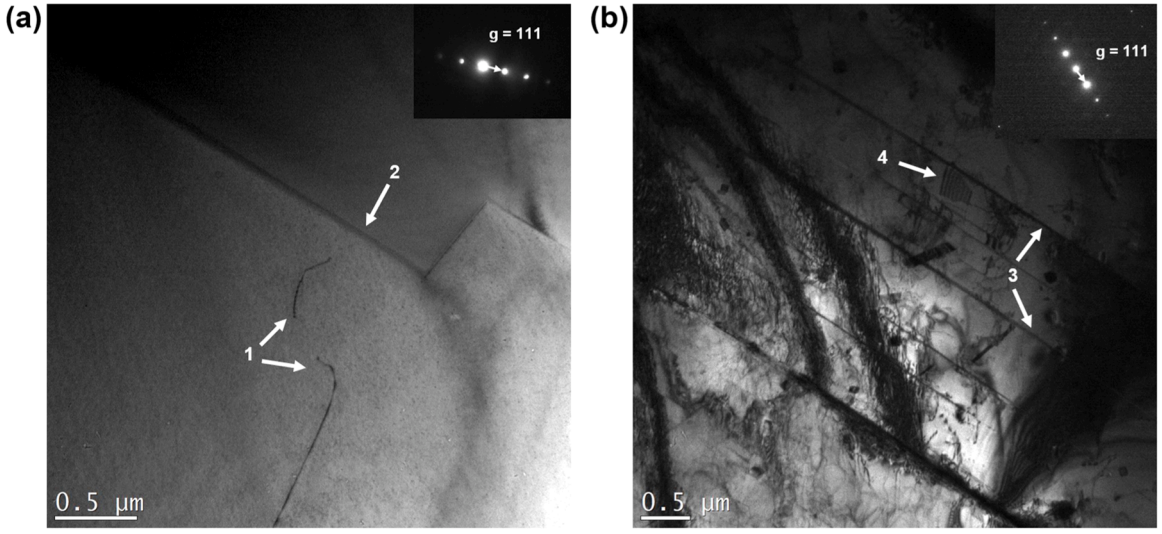

Fig. 8. Dislocation structure prior to creep testing of (a) wrought CrCoNi showing two dislocations (arrows 1) and a twin boundary (arrow 2) and (b) AM CrCoNi showing a high dislocation density, (111) slip traces (arrows 3), and stacking faults (arrow 4).

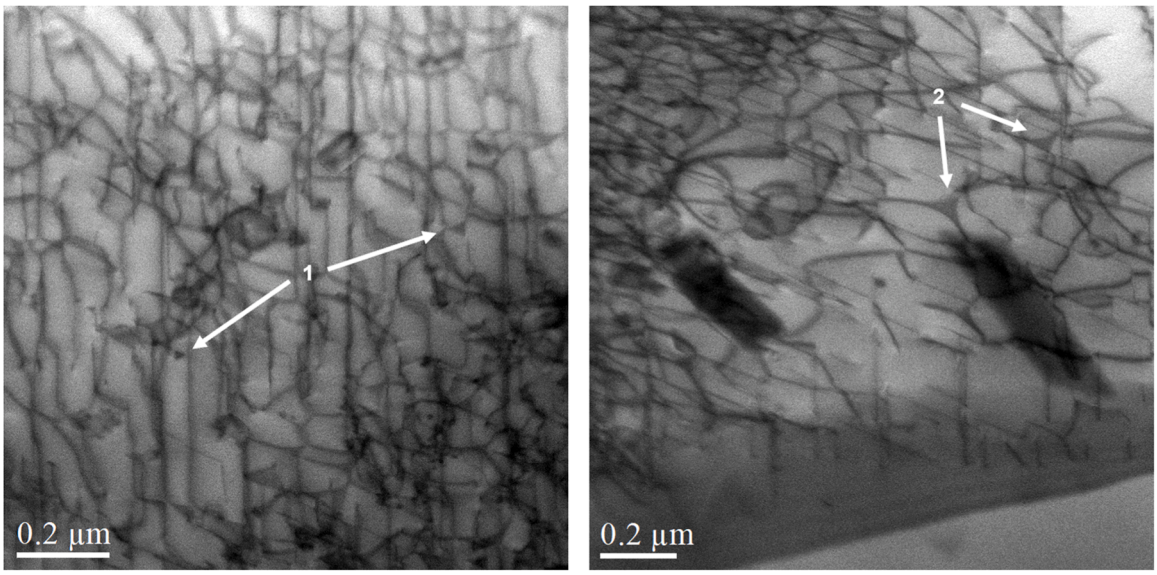

Fig. 9. DCI-STEM images of the dislocation structure of uncrept AM CrCoNi showing a dislocation network, stacking fault tetrahedra (arrows 1), and extended nodes (arrows 2).

Figs. 10–12, which show the dislocation structures of both materials crept to steady state. Instead, the individual dislocations are broadly curved and form multijunctions and jogs. Multijunctions are associated with dislocation bowing from forest dislocation interactions and particles in the AM material. These arrangements are similar to the dislocation structures observed in the Cantor alloy crept to steady state [10]. Slip bands blocked by boundaries are observed in Figs. 10 and 12; these slip bands were not observed in the Cantor alloy. No evidence of slip band emission from grain boundaries was observed. Additionally, these blocked slip bands occur more frequently in the AM material. As seen in Fig. 10, there are two sets of diffraction spots visible indicating that this is a twin boundary. Also, unlike the Cantor alloy, the dislocation structures of CrCoNi are not consistent with the room and cryogenic temperature dislocation structures. The structure of wrought CrCoNi deformed at room and cryogenic temperatures is characterized by the glide of dislocations dissociated into Shockley partials with stacking faults in between, and nanotwinning [33]. Some dislocations dissociated into Shockley partials connected by stacking faults are observed in Fig. 12, but these are much fewer in number than in the typical dislocation structures observed following room and cryogenic temperature deformation. Nanotwins are not expected to form at the relatively low stresses involved in creep tests, and indeed none were observed [34].

3.4. Particle characterization in AM CrCoNi

Figs. 8(b), 9, 11, and 12, reveal that spherical and cuboidal particles are present in the AM CrCoNi. STEM-EDS of the particles, as shown in Fig. 13, indicates that they are Cr-rich oxides which have also been observed in wrought CrCoNi by other authors [35,36]. There are three distinct oxides in the AM material shown in Fig. 13. These oxides are classified as bright cuboidal, dark cuboidal, and dark spherical based on their physical appearance. The compositions of these oxides are reported in Fig. 13 and reveal that the bright cuboidal oxides are Cr_2O_3 while the other two are Cr-rich complex oxides. As observed qualitatively in the

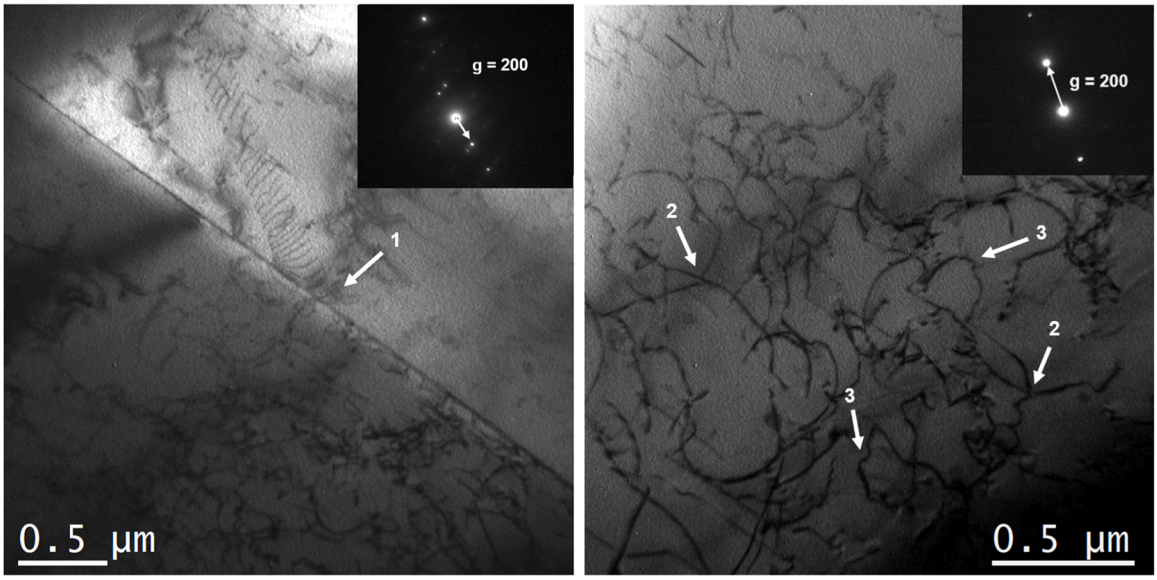

Fig. 10. TEM images of dislocation structures in wrought CrCoNi crept to steady state at 1023 K and 80 MPa showing a slip band blocked by a twin boundary (arrow 1), multijunctions (arrows 2), and jogs (arrows 3).

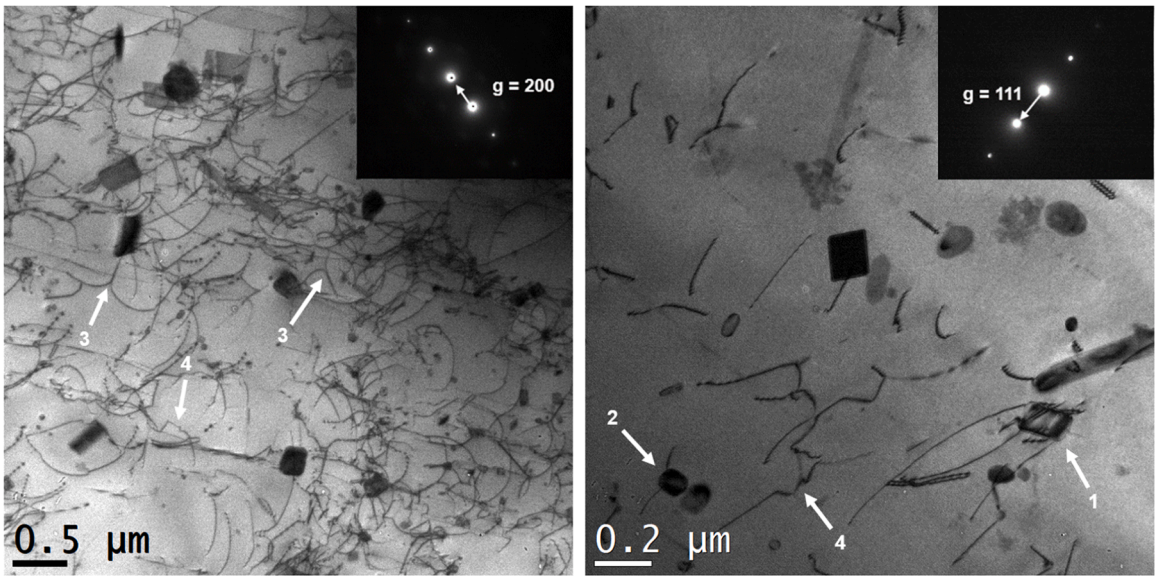

Fig. 11. TEM images of the dislocation structure in AM CrCoNi crept to steady state at 1023 K and 80 MPa, showing dislocation nucleation at an incoherent Cr_2O_3/CrCoNi matrix interface (arrow 1), dislocation interactions with oxides such as detachment (arrow 2), multijunctions (arrows 3), and jogs (arrows 4).

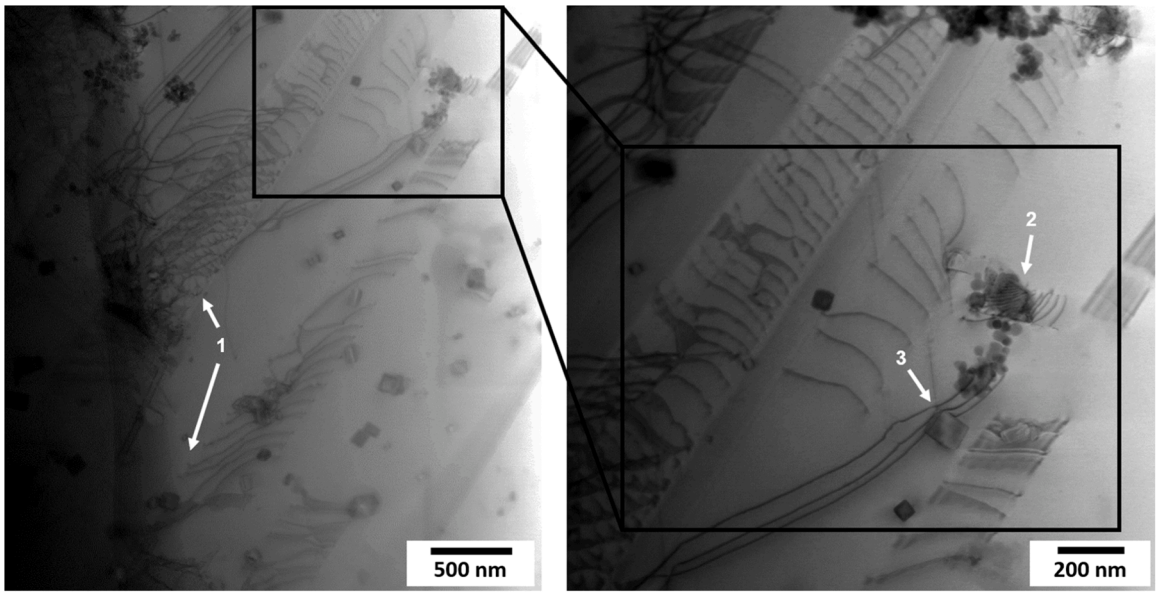

Fig. 12. DCI-STEM images of the dislocation structure in AM CrCoNi crept to steady state at 1023 K and 80 MPa, showing slip bands blocked by a grain boundary (arrows 1), dislocation generation at an incoherent Cr_2O_3/CrCoNi matrix interface (arrow 2), and dislocation interactions with oxides such as bowing (arrow 3).

TEM images (Figs. 8–12), the fraction of Cr-rich oxides in AM CrCoNi is much higher than in the wrought material, likely due to the oxygen present on the powders prior to AM processing. It has also been speculated that oxygen take-up occurs during laser melting because of the presence of oxygen in the chamber [37]. The total area fraction of Cr-rich oxides in the AM material was found to be 4 % as determined by area measurements of 140+ particles over a total area of 74 μm^2 using ImageJ. Assuming a uniform distribution of particles, the oxide volume fraction is calculated to be 0.6 %. These incidental Cr-rich oxides are another possible contributor to the superior creep resistance in the AM CrCoNi compared to wrought. Fig. 11 illustrates that dislocations tend to cluster near the oxides even though creep subgrains do not form. Individual dislocations can also be seen interacting with particles in Figs. 11 and 12, both piling up at them and apparently detaching from them as in the Rösler-Arzt model. These processes are characteristic of the rate-controlling processes in dispersion strengthened metals [38–41]. In addition, the Cr_2O_3/CrCoNi matrix interface is incoherent and serves as a source of dislocations, as observed in Figs. 11 and 12, which is also observed in ODS alloys [42]. The dislocation/oxide interactions are not widespread and thus likely are not the primary deformation rate-controlling mechanism in the AM material. However, the oxides limit the glide distance of mobile dislocations after overcoming an obstacle and thus contribute to the lower steady state creep rates in the AM alloy. Additionally, these interactions may still inhibit creep deformation and thereby increase creep resistance in the AM CrCoNi, despite the present alloy not being designed to include strengthening particles.

3.5. Fracture characteristics after creep in wrought and AM CrCoNi

The average creep ductilities of wrought and AM CrCoNi were 17.5

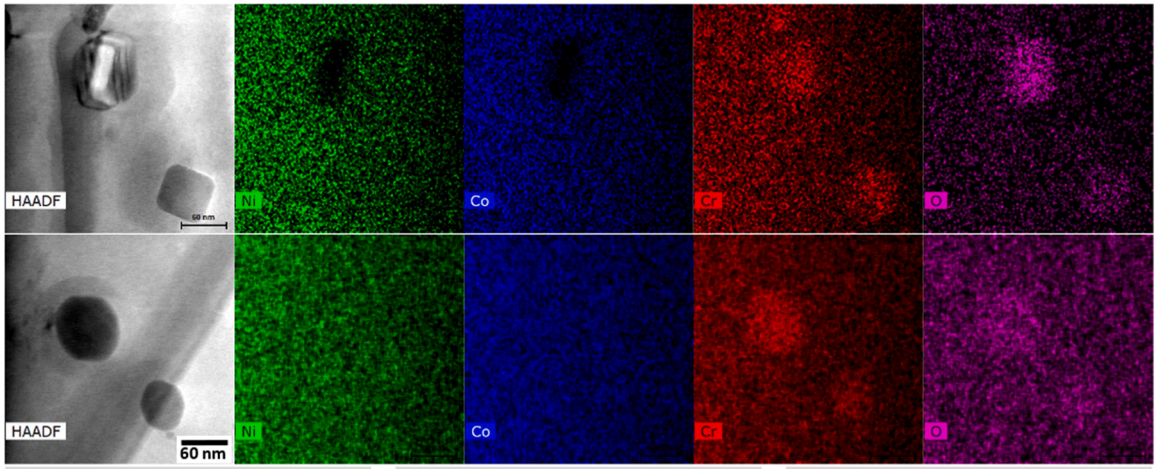

Bright Cuboidal		Dark Cuboidal		Dark Spherical	
Element	Atomic %	Element	Atomic %	Element	Atomic %
Cr	37.62	Cr	40.24	Cr	39.21
O	59.26	O	32.42	O	9.84
Co	1.88	Co	13.82	Co	25.86
Ni	1.24	Ni	13.52	Ni	25.10

Fig. 13. STEM-EDS of Cr-rich oxides in AM CrCoNi and their corresponding atomic percentage.

± 1.9 % and 7.2 ± 0.8 %, respectively. The lower creep ductility of the AM material stems from (1) the higher volume fraction of oxides acting as cavity nucleation sites, (2) the lower LAGB length percentage limiting easy propagation of deformation across grain boundaries, and (3) the higher TB length percentage limiting the number of dislocation source at boundaries, thereby reducing the possibility of slip transmission on the other side of the boundary. Trace impurity levels are similar in the two materials (except for the oxygen that forms oxides in the AM material), hence cannot explain the difference in ductility. It is well known that, during creep deformation, dislocation pile-ups against GBs (Zener-Stroh mechanism), as well as hard particles on GBs lead to the nucleation of voids which coalesce and result in intergranular fracture [43–47]. As demonstrated by Dyson, creep ductility decreases as the rate of cavity production increases [48]. The fracture surfaces of wrought and AM CrCoNi in Fig. 14 illustrate that the higher volume fraction of oxides in the AM material causes numerous small cavities to nucleate, which then coalesce leading to fracture at a lower ductility than the wrought material. Additionally, the lower LAGB length percentage in the AM material causes the Zener-Stroh mechanism to be more prevalent than in the wrought material. Since dislocation pile-ups are more likely to propagate through LAGBs, Zener-Stroh induced cavities are less likely to nucleate in the wrought material. However, since the LAGB length percentage in the YZ plane is 0.9 % in the AM material and 3.2 % in the wrought material, the oxides in the AM material likely make a larger contribution to its lower ductility than the Zener-Stroh mechanism.

Fig. 15 shows the surfaces of fractured specimens of both materials and verifies the intergranular fracture that is characteristic of creep deformation and the previous description. Additionally, much more extensive cracking is observed on the polished face of the wrought CrCoNi compared to the AM material. This difference reflects the higher creep ductility (and damage tolerance) of the wrought material and is consistent with its larger tertiary creep regime compared to the AM material (Fig. 4). The difference in the amount of cracking before failure is shown for another combination of temperature and applied stress in Fig. S3. Fig. S4 illustrates a comparison of the wrought and AM material

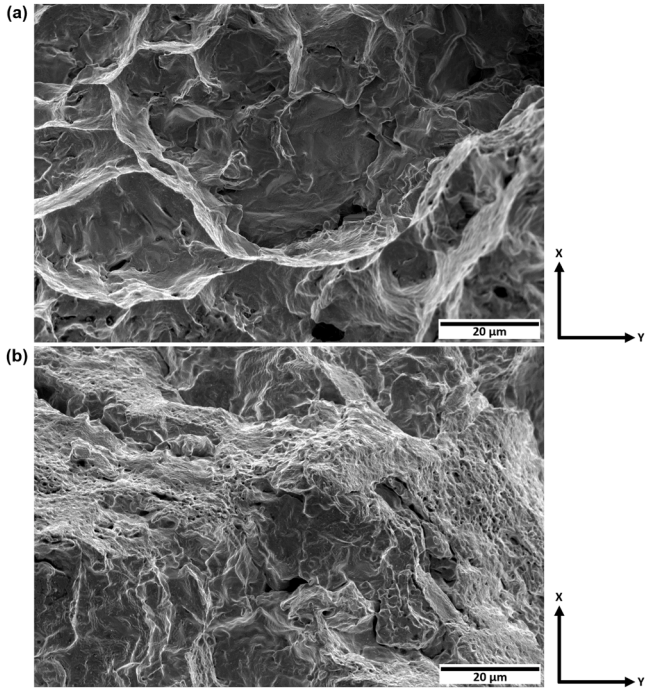

Fig. 14. Fracture surfaces of (a) wrought CrCoNi and (b) AM CrCoNi following creep rupture at 1023 K and 130 MPa.

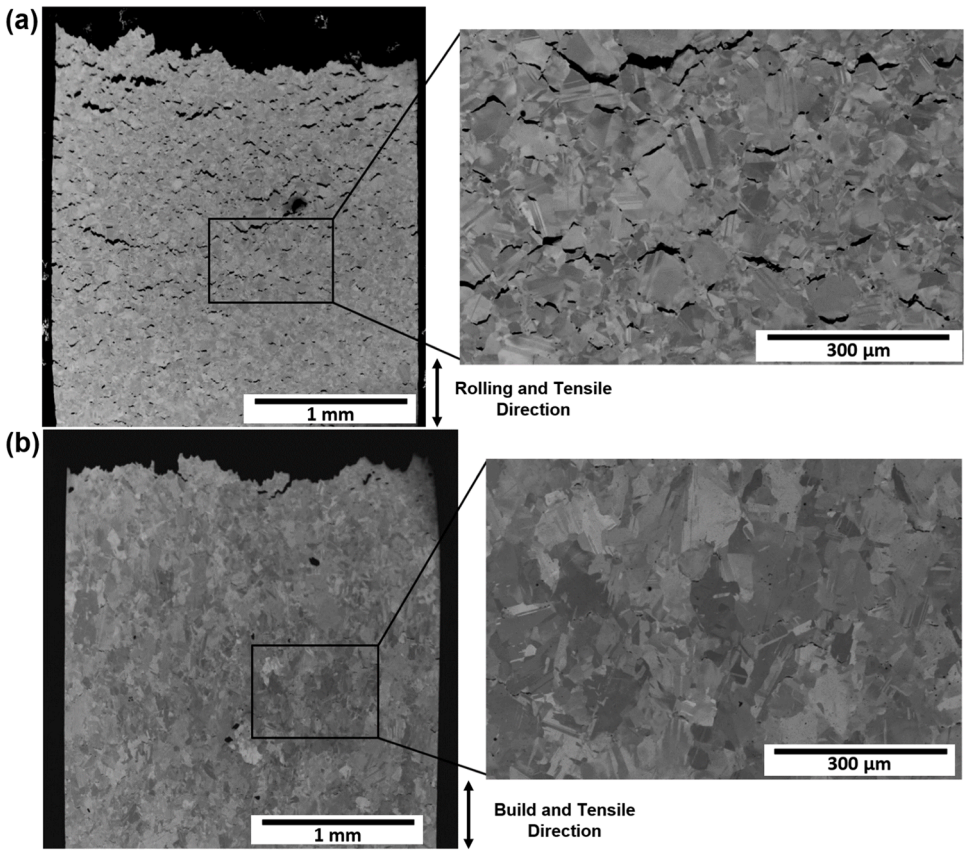

Fig. 15. Surfaces of specimens following creep rupture at 1023 K and 80 MPa for (a) wrought CrCoNi and (b) AM CrCoNi.

crept to 4 % strain. This is in the middle of steady state creep for the AM material and at the beginning of steady state creep for the wrought material. As shown, there is minimal cracking in both materials at 4 % strain indicating that most of the cracking occurs during tertiary creep. Additionally, an EBSD map of the fractured wrought material shown in Fig. 15 is presented in Fig. S5 from which it can be observed that cracks do not form at TBs. It is important to note that since creep failure occurs by intergranular fracture, and cracks do not form at TBs, the number and type of transverse grain boundaries strongly influence creep ductility. Despite the attempt to minimize differences in grain size of the two materials, the elongated grains in the build direction of the AM material lead to fewer transverse grain boundaries compared to the wrought material which should be beneficial to the creep ductility of the AM material. However, as observed from the fracture surfaces (Fig. 14), the higher volume fraction of oxides dominates the creep fracture behavior and limits ductility in the AM material.

The high initial dislocation density of the AM material could also contribute to its lower creep ductility; however, these dislocations annihilate during furnace heating and stabilization before creep testing, which takes 3.5 h. Fig. S6 shows that there is a minimal number of dislocations in the AM material after annealing at 1073 K for 6 h (which is slightly longer than the normal heat-up period). Fig. S7 presents a log-log plot of steady state creep rate vs applied stress for the annealed and non-annealed AM material demonstrating that the steady state creep rates are unaffected by annealing. Additionally, creep ductilities for annealed and non-annealed AM CrCoNi were found to be within 1 % for each set of testing parameters. These results show that the annealed and non-annealed AM material have nearly identical creep resistance and creep ductility, confirming that the high initial dislocation density of the AM material does not affect the creep behavior for the given testing procedures. The BSE SEM image in Fig. S8 shows the grain morphology of the annealed AM material with crystallite size of 16.8 ± 2.3 μm in the Z-direction of the YZ plane and 14.9 ± 2.3 μm in the Y-direction of the YZ plane. The annealing process allowed the crystallites to become more equiaxed; however the average size has not changed, suggesting that the crystallites in the HIPed AM material have achieved a stable size [49, 50].

In a similar comparison of the high temperature properties of wrought and additively manufactured nickel-base alloy IN625, Son, et al. [51] observed that Mg is commonly added to this alloy to tie-up S. Their results showed that Mg was vaporized during AM, leading to a lower concentration in the alloy and suggesting that S was free to act as an embrittling element. In the present study, the S content is much lower than in the alloy studied by Son, et al. and below the threshold that they suggested as the limit below which embrittlement is not of concern [51]. Furthermore, the S and Mg content of both alloys tested in the present study are essentially the same, as shown in Table 1. From these observations, we conclude that S embrittlement cannot explain the differences in creep ductilities between wrought and AM CrCoNi.

3.6. Comparison of creep behaviors

A comparison of creep data for CrCoNi and Cantor alloy is shown in Table 3. As discussed earlier, the activation energies of AM CrCoNi, wrought CrCoNi, and Cantor alloy are sequentially lower, reflecting differences in their respective creep resistance at a given stress and temperature. However, the activation energy values for wrought CrCoNi from Xie, et al. [35] exceed those for both the wrought and AM CrCoNi of this study. This is likely due to the use of a constant load technique in their study as opposed to the constant stress technique used in the present study and that of Zhang, et al. [10] as well as the significantly larger grain size of the material used in the study by Xie, et al.

One approach is to consider the AM material to be composite strengthened by non-deformable particulates. An approach by Hong and

Table 3
Comparison of Creep Data for CrCoNi and Cantor Alloy.

Study	GRAIN SIZE (mm)	n	Q_C (kJ/mol)	T RANGE (K)	σ RANGE (MPa)
Wrought CrCoNi (THIS STUDY)	31.2 ± 1.9	4.5 ± 0.2	240–259	1023–1173	40–200
AM CrCoNi (THIS STUDY)	57.9 ± 2.5	5.9 ± 0.1	320–331	1023–1173	40–200
Wrought CrCoNi [35]	149 ± 4	5.3 ± 0.2	370	973–1073	30–130
Wrought CrMnFeCoNi [10]	24 ± 12	3.7 ± 0.1	219–236	1023–1173	20–200

Chung [52] is adopted as given by Eq. (2), which is a simplified version of the Nardone and Prewo model [53]. Eq. (2) has also been used by Zhang, et al. for a similar purpose to describe creep deformation in a rapidly solidified Al–Fe–V–Si alloy [54].

$$\sigma_{eff} = \sigma\left[1 - \frac{f \times \left(\frac{S}{2}+1\right)}{f \times \left(\frac{S}{2}+1\right) + (1-f)}\right] \quad (2)$$

In this expression, σ_{eff} is the effective stress after accounting for the portion of the load carried by the particles, f is the volume fraction of particles in the material, and S is the aspect ratio of the particles. It can be observed that the use of σ_{eff} with constant f and S will simply shift the log-log steady state creep rate vs applied stress plot along the stress axis without changing its slope. While the oxides may carry a portion of the applied load and thus lower steady state creep rates of the AM alloy matrix, the different slopes (different values of n) between the AM and wrought CrCoNi cannot be explained by this simple composite approach.

Another important point regarding differences in creep rates and stress exponents in both materials is that stress exponents for ODS alloys in which dislocation/particle interactions control the deformation rate typically range from 10 to 50 [55,56], with single crystal ODS alloys reaching stress exponents as high as 75 [57]. Clearly, the stress exponent of 5.9 ± 0.1 of the AM CrCoNi, although slightly greater than is typical for power law creep in pure metals, does not compare with these high values commonly found in ODS alloys. Hence, a climb or bowing mechanism to overcome the oxides is ruled out as a primary cause for the better creep resistance and different stress dependence of the AM material. Furthermore, the large size (approximately 100 nm) and low volume fraction of oxides in the AM material (0.6 %) are generally not in the range of values in which climb over particles, bowing between particles, or dislocation detachment are expected to be rate controlling processes. Additionally, as observed in Figs. 11 and 12, two Cr_2O_3 particles appear to generate dislocations at the particle/matrix interface. This dislocation nucleation as well as dislocations interacting with and clustering around oxide particles certainly contribute to the creep strength of the AM material, but only isolated instances of dislocation bowing or climb were found in the present study.

In summary, the lower steady state creep rate in the AM material compared to wrought is attributed to a combination of a larger volume fraction of oxides in AM CrCoNi which interact with dislocations and limit the area swept by gliding dislocations after release from an obstacle, the fact that these oxide particles carry a portion of the applied load, and the lower length percentage of the relatively weak LAGB in the AM material.

4. Conclusions

A comparative study of the influence of processing methods on the creep properties of a CrCoNi MPEA was conducted. Material was tested in the annealed vacuum arc melted and HIPed additively manufactured conditions and both were chemically and microstructurally characterized to observe differences contributing to their distinct creep behaviors. Constant stress creep tests were performed on both materials in the ranges of 1023–1173 K and 40–200 MPa. TEM was used to observe the steady state creep behavior and BSE SEM was used to characterize the fracture behavior in these materials.

1 Stress exponents of 4.5 ± 0.2 and 5.9 ± 0.1 and activation energies ranging from 240 to 259 and 320–331 kJ/mol were found for wrought and AM CrCoNi, respectively. These stress exponents are in the range commonly associated with the dislocation climb mechanism of creep deformation, although no creep subgrains were observed in the CrCoNi as would be expected for typical metals with stress exponents in this range.
2 Cr-rich oxides were observed in the AM material in greater numbers than in the wrought material. The incoherent Cr_2O_3/matrix interface results in the generation of dislocations. Interactions of gliding dislocations with these oxide particles are not rate controlling, although the ability of these particles to bear a portion of the applied load may contribute to the increased creep resistance of the AM material. Additionally, these oxides contribute to the lower steady state creep rates of the AM alloy by limiting the glide distance of mobile dislocations after overcoming an obstacle.
3 A lower LAGB length percentage was found in the AM material compared to wrought. Since more energy is required for a dislocation to move through TBs and HAGBs than LAGBs, this difference also leads to increased creep resistance of the AM material.
4 Both CrCoNi materials have better creep resistance than CrMnFeCoNi (Cantor alloy) at similar stresses and temperatures. The steady state dislocation structures were similar in both CrCoNi materials with individual curved dislocations with dislocation multijunctions and jogs, similar to the Cantor alloy. However, slip bands, which have not been reported in the Cantor alloy after creep, were observed in the CrCoNi. Neither material exhibited subgrains which are typical of pure polycrystalline FCC metals.
5 The average creep ductilities were 17.5 ± 1.9 % and 7.2 ± 0.8 % for wrought and AM CrCoNi, respectively. The higher volume fraction of oxides in the AM material provided additional cavity nucleation sites leading to more rapid void coalescence and consequent fracture. The lower number of dislocation pile-ups in the wrought material suggests that the higher LAGB length percentage allowed deformation to propagate more readily, reducing cavity nucleation at GBs and prolonging creep life. In addition, the higher TB length percentage limits the number of dislocation sources, thereby reducing the possibility of slip transmission on the other side of the boundary. The difference in creep ductility was reflected by a larger amount of stable cracking before fracture in the wrought material.

Declaration of Competing Interest

The authors declare that they have no known competing financial interests or personal relationships that could have appeared to influence the work reported in this paper.

Acknowledgements

Partial funding for this research was provided by the University of California, Davis and by donations to the Department of Materials Science and Engineering. A portion of this study was carried out at the UC Davis Center for Nano- and Micro-Manufacturing (CNM2). Funding for the Thermo Fisher Quattro S was provided by NSF grant No. DMR-1725618. Work at the Molecular Foundry (M.Z. and A.M.M.) was supported by the U. S. Department of Energy, Office of Science, Office of Basic Energy Sciences under Contract No. DE-AC02–05CH11231. Partial funding for this study was provided by NASA's Aeronautics Research Mission Directorate (ARMD) – Transformational Tools and Technologies (TTT) Project Office. Research at Oak Ridge National Laboratory (E.P. G.) was supported by the U.S. Department of Energy, Office of Science, Basic Energy Sciences, Materials Sciences and Engineering Division.

Supplementary materials

Supplementary material associated with this article can be found, in the online version, at doi:10.1016/j.actamat.2023.119403.

References

[1] F. Otto, A. Dlouhy, C. Somsen, H. Bei, G. Eggeler, E.P. George, The influences of temperature and microstructure on the tensile properties of a CoCrFeMnNi high-entropy alloy, Acta Mater 61 (2013) 5743–5755.
[2] B. Gludovatz, A. Hohenwarter, K.V.S. Thurston, H. Bei, Z. Wu, E.P. George, R. O. Ritchie, Exceptional damage-tolerance of a medium-entropy alloy CrCoNi at cryogenic temperatures, Nat Commun 7 (2016) 10602.
[3] G. Laplanche, A. Kostka, O.M. Horst, G. Eggeler, E.P. George, Microstructure evolution and critical stress for twinning in the CrMnFeCoNi high-entropy alloy, Acta Mater 118 (2016) 152–163.
[4] J. Miao, C.E. Slone, T.M. Smith, C. Niu, H. Bei, M. Ghazisaeidi, G.M. Pharr, The evolution of the deformation substructure in a Ni-Co-Cr equiatomic solid solution alloy, Acta Mater 132 (2017) 35–48.
[5] F.D.G. Filho, R.O. Ritchie, M.A. Meyers, Cantor-derived medium-entropy alloys: bridging the gap between traditional metallic and high-entropy alloys, J Mater Res Technol 17 (2022) 1868–1895.
[6] Z. Wu, H. Bei, G.M. Pharr, E.P. George, Recovery, recrystallization, grain growth and phase stability of a family of FCC-structured multi-component equiatomic solid solution alloys, Intermetallics 46 (2014) 131–140.
[7] A. Gali, E.P. George, Tensile properties of high- and medium-entropy alloys, Intermetallics 39 (2013) 74–78.
[8] J.Y. He, C. Zhu, D.Q. Zhou, W.H. Liu, T.G. Nieh, Z.P. Lu, Steady state flow of the FeCoNiCrMn high entropy alloy at elevated temperatures, Intermetallics 55 (2014) 9–14.
[9] C. Cao, J. Fu, T. Tong, Y. Hao, P. Gu, H. Hao, L. Peng, Intermediate-temperature creep deformation and microstructural evolution of an equiatomic FCC-structured CoCrFeNiMn high-entropy alloy, Entropy 20 (12) (2018) 960.
[10] M. Zhang, E.P. George, J.C. Gibeling, Tensile creep properties of a CrMnFeCoNi high-entropy alloy, Scr Mater 194 (2021), 113633.
[11] J.Y. He, H. Wang, H.L. Huang, X.D. Xu, M.W. Chen, Y. Wu, X.J. Liu, T.G. Nieh, K. An, Z.P. Lu, A precipitation-hardened high-entropy alloy with outstanding tensile properties, Acta Mater 102 (2016) 187–196.
[12] H. Shahmir, M. Nili-Ahmadabadi, A. Shafiee, T.G. Langdon, Effect of a minor titanium addition on the superplastic properties of a CoCrFeNiMn high-entropy alloy processed by high-pressure torsion, Mater. Sci. Eng. A 718 (2018) 468–476.
[13] Z. Fu, L. Jiang, J.L. Wardini, B. MacDonald, H. Wen, W. Xiong, D. Zhang, Y. Zhou, T.J. Rupert, W. Chen, E.J. Lavernia, A high-entropy alloy with hierarchical nanoprecipitates and ultrahigh strength, Sci Adv 4 (10) (2018).
[14] A. Hoffman, L. He, M. Luebbe, H. Pommerenke, J. Duan, P. Cao, K. Sridharan, Z. Lu, H. Wen, Effects of Al and Ti additions on irradiation behavior of FeMnNiCr multi-principal-element alloy, JOM 72 (2020) 150–159.
[15] D.A. Santana, K.R. Santos, C.S. Kiminami, F.G. Coury, Design, phase equilibria, and coarsening kinetics of a new γ/γ' precipitation-hardened multi-principal element alloy, J Alloys Compd 882 (2021), 160729.
[16] H. Hadraba, Z. Chlup, A. Dlouhy, F. Dobes, P. Roupcova, M. Vilemova, J. Matejicek, Oxide dispersion strengthened CoCrFeNiMn high-entropy alloy, Mater. Sci. Eng. A 689 (2017) 252–256.
[17] T.M. Smith, A.C. Thompson, T.P. Gabb, C.L. Bowman, C.A. Kantzos, Efficient production of a high-performance dispersion strengthened, multi-principal element alloy, Sci Rep 10 (2020) 9663.
[18] D. Yang, Y. Liu, N. Qu, T. Han, M. Liao, Z. Lai, J. Zhu, Effect of fabrication methods on microstructures, mechanical properties and strengthening mechanisms of Fe0.25CrNiAl medium-entropy alloy, J Alloys Compd 888 (2021), 161526.
[19] F. Otto, N.L. Hanold, E.P. George, Microstructural evolution after thermomechanical processing in an equiatomic, single-phase CoCrFeMnNi high-entropy alloy with special focus on twin boundaries, Intermetallics 54 (2014) 39–48.
[20] S.E. Broyles, M. Zhang, J.C. Gibeling, Influence of annealing on the creep behavior of GlidCop Al-15, Mater. Sci. Eng. A 779 (2020), 139112.
[21] M.W. Decker, J.R. Groza, J.C. Gibeling, Creep properties of an extruded copper-8% chromium-4% niobium alloy, Mat Sci Eng A Struct 369 (1–2) (2004) 101–111.
[22] C.E. Slone, J. Miao, E.P. George, M.J. Mills, Achieving ultra-high strength and ductility in equiatomic CrCoNi with partially recrystallized microstructures, Acta Mater 165 (15) (2019) 496–507.
[23] S. Liu, D. Wan, S. Guan, Y. Fu, X. Ren, Z. Zhang, J. He, Microstructure and nanomechanical behavior of an additively manufactured (CrCoNiFe)94Ti2Al4 high-entropy alloy, Mater. Sci. Eng. A 823 (17) (2021), 141737.
[24] G.D. Sathiaraj, W. Skrotzki, A. Pukenas, R. Schaarschuch, R.J. Immanuel, S. K. Panigrahl, J.A. Chelvan, S.S.S. Kumar, Effect of annealing on the microstructure and texture of cold rolled CrCoNi medium-entropy alloy, Intermetallics 101 (2018) 87–98.
[25] M. Schneider, E.P. George, T.J. Manescau, T. Zalezak, J. Hunfeld, A. Dlouhy, G. Eggeler, G. Laplanche, Analysis of strengthening due to grain boundaries and annealing twin boundaries in the CrCoNi medium-entropy alloy, Int. J. Plast. 124 (2020) 155–169.
[26] O.D. Sherby, P.M. Burke, Mechanical behavior of crystalline solids at elevated temperature, Prog Mater Sci 13 (1968) 323–390.
[27] K. Jin, C. Zhang, F. Zhang, H. Bei, Influence of compositional complexity on interdiffusion in Ni-containing concentrated solid-solution alloys, Mater. Res. Lett. (2018) 293–299.
[28] S. Sun, W. Zai, Y. Chen, G. Sun, J. Hu, S. Han, J. Lian, Effects of cold-rolling and subsequent annealing on the nano-mechanical and creep behaviors of CrCoNi medium-entropy alloy, Mater. Sci. Eng. A 839 (2022), 142802.
[29] S. Chen, Q. Yu, The role of low angle grain boundary in deformation of titanium and its size effect, Scr Mater 163 (2019) 148–151.
[30] F. Habiyaremye, A. Guitton, F. Schafer, F. Scholz, M. Schneider, J. Frenzel, G. Laplanche, N. Maloufi, Plasticity induced by nanoindentation in a CrCoNi medium-entropy alloy studied by accurate electron channeling contrast imaging revealing dislocation-low angle grain boundary interactions, Mater. Sci. Eng. A 817 (2021), 141364.
[31] J. Silcox, P.B. Hirsch, Direct observations of defects in quenched gold, Philos Mag 4 (37) (1959) 72–89.
[32] O.D. Sherby, R.H. Klundt, A.K. Miller, Flow stress, subgrain size, and subgrain stability at elevated temperature, Metall. Trans. A 8 (1977) 843–850.
[33] G. Laplanche, A. Kostka, C. Reinhart, J. Hunfeld, G. Eggele, E.P. George, Reasons for the superior mechanical properties of medium-entropy CrCoNi compared to high-entropy CrMnFeCoNi, Acta Mater 128 (2017) 292–303.
[34] H. Huang, X. Li, Z. Dong, W. Li, S. Huang, D. Meng, X. Lai, T. Liu, S. Zhu, L. Vitos, Critical stress for twinning nucleation in CrCoNi-based medium and high entropy alloys, Acta Mater 149 (2018) 388–396.
[35] D. Xie, R. Feng, P.K. Liaw, H. Bei, Y. Gao, Tensile creep behavior of an equiatomic CoCrNi medium entropy alloy, Intermetallics 121 (2020), 106775.
[36] M.P. Agustianingrum, U. Lee, N. Park, High-temperature oxidation behaviour of CoCrNi medium-entropy alloy, Corros Sci 173 (2020), 108755.
[37] K. Saeidi, X. Gao, Y. Zhong, Z.J. Shen, Hardened austenite steel with columnar sub-grain structure formed by laser melting, Mater. Sci. Eng. A 625 (2015) 221–229.
[38] R. Lagneborg, Bypassing of dislocations past particles by a climb mechanism, Scr. Metall. 7 (6) (1973) 605–614.
[39] W. Blum, B. Reppich, Creep of particle-strengthened alloys, Creep Behav. Crystal. Solids (1985) 83–135.
[40] J. Rösler, E. Arzt, A new model-based creep equation for dispersion strengthened materials, Acta Metall. Mater. 38 (4) (1990) 671–683.
[41] M. Zhang, J.C. Gibeling, Understanding creep mechanisms of a Cu-Cr-Nb alloy by testing under constant structure conditions, Scr Mater 190 (2021) 131–135.
[42] L.M. Brown, G.R. Woolhouse, The loss of coherency of precipitates and the generation of dislocations, Philosoph. Magaz. A J. Theor. Exp. Appl. Phys. 8 (1970) 329–345.
[43] F.A. McClintok, A criterion for ductile fracture by the growth of holes, J Appl Mech 35 (2) (1968) 363–371.
[44] R. Lombard, H. Vehoff, Nucleation and growth of cavities at defined grain boundaries in bicrystals, Scr. Metall. 24 (3) (1990) 581–586.
[45] E.P. George, R.L. Kennedy, D.P. Pope, Review of trace element effects on high-temperature fracture of Fe- and Ni-base alloys, Phys. Status Solidi A 167 (2) (1998) 313–333.
[46] Y.S. Lee, J. Yu, Effect of matrix hardness on the creep properties of a 12CrMoVNb steel, Metall. Mater. Trans. A 30A (1999) 2331–2339.
[47] M.E. Kassner, T.A. Hayes, Creep cavitation in metals, Int. J. Plast. 19 (10) (2003) 1715–1748.
[48] B.F. Dyson, Continuous cavity nucleation and creep fracture, Scr. Metall. 17 (1) (1983) 31–37.
[49] M. Hillert, On the theory of normal and abnormal grain growth, Acta Metall. 13 (3) (1965) 227–238.

[50] H.V. Atkinson, Overview no. 65: theories of normal grain growth in pure single phase systems, Acta Metall. 36 (3) (1988) 469–491.
[51] K.T. Son, T.Q. Phan, L.E. Levine, K.S. Kim, K.A. Lee, M. Ahlfors, M.E. Kassner, The creep and fracture properties of additively manufactured inconel 625, Materialia 15 (2021), 101021.
[52] S.H. Hong, K.H. Chung, High temperature creep behavior of SiC/2124Al metal matrix composites, Key Eng. Mater. 104-107 (1995) 757–764.
[53] V.C. Nardone, K.M. Prewo, On the strength of discontinuous silicon carbide reinforced aluminum composites, Scr. Metall. 20 (1986) 43–48.
[54] M. Zhang, R.J. Lewis, J.C. Gibeling, Mechanisms of creep deformation in a rapidly solidified Al–Fe–V–Si alloy, Mater. Sci. Eng. A 805 (2021), 140796.
[55] V.C. Nardone, J.K. Tien, On the creep rate stress dependence of particle strengthened alloys, Scr. Metall. 20 (1986) 797–802.
[56] S.E. Broyles, K.R. Anderson, J.R. Groza, J.C. Gibeling, Creep deformation of dispersion-strengthened copper, Metall. Mater. Trans. A 27 (1996) 1217–1227.
[57] R.W. Lund, W.D. Nix, High temperature creep of Ni-20Cr-2ThO2 single crystals, Acta Metall. 24 (5) (1976) 469–481.